Biocorrosion on Nanofilms Induces Rapid Bacterial Motions via Iron Dissolution

Marion Lherbette, Christophe Regeard, Christian Marlière, and Eric Raspaud*
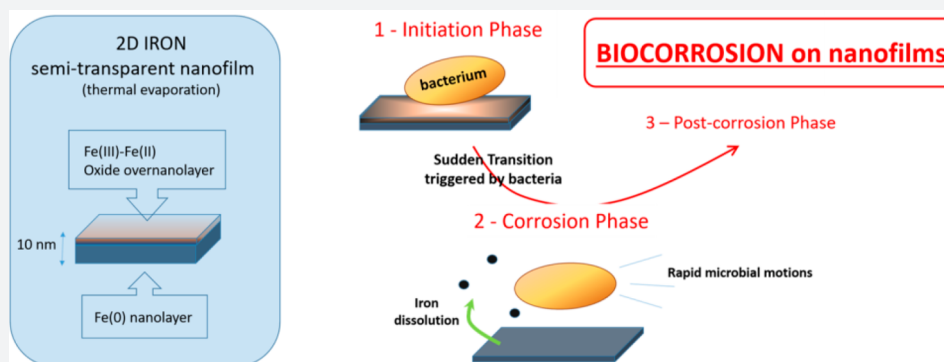
Read Online

ACCESS | Metrics & More | Article Recommendations | Supporting Information

ABSTRACT: Stability and reactivity of solid metal or mineral surfaces in contact with bacteria are critical properties for development of biocorrosion protection and for understanding bacteria–solid environmental interactions. Here, we opted to work with nanosheets of iron nanolayers offering arbitrarily large and stable areas of contact that can be simply monitored by optical means. We focused our study on the sediments' bacteria, the strain *Shewanella oneidensis WT* MR-1, that served as models for previous research on electroactivity and iron-reduction effects. Data show that a sudden uniform corrosion appeared after an early electroactive period without specific affinities and that iron dissolution induced rapid bacterial motions. By extending the approach to mutant strains and three bacterial species, we established a correlation between corrosion onset and oxygen-depletion combined with iron reduction and demonstrated bacteria's extraordinary ability to transform their solid environments.

■ INTRODUCTION

Iron is an abundant element found mostly in the two Fe(II) and Fe(III) states in the Earth's crust. Like most living cells that internalize (assimilate) iron for their optimal functioning (homeostasis), some prokaryotic organisms, like the dissimilatory metal-reducing bacteria, are also able to utilize environmental and external iron for their own respiration. Cells have adopted different evolutionary strategies to exploit sources of iron in which low solubility at neutral pH reduces availability.[1] Reactivity and stability of interfacial mineral nanolayers are therefore crucial properties involved in the regulation of life evolution in soils and in different processes of nanomineralogy and nanogeoscience.[2,3]

Corrosion is driven by multiple electrochemical reactions on metal surfaces, and nanocoatings are among the current approaches of nanotechnology to prevent reactions. Microbially influenced corrosion (MIC) refers more specifically to the corrosion involving microorganisms.[4–6] Given the variety of microbes, metals, and media, MIC involves a myriad of interactions, chemical reactions, and mechanisms.[5,7] As microorganisms actively change the local physical/chemical state of solid metal and its surrounding liquid medium, their presence is most often associated with localized pitting corrosion (see refs 7–9 and references therein). Microorganisms catalyze (initiate/accelerate) local corrosions, separating spatially reduction from oxidation sites along the metal surface. This type of corrosion completely differs from unlocalized corrosion, another well-known type of corrosion. In the latter case, the metal surface degrades uniformly and homogeneously. Though being the subject of extensive research for more than a century[10] and the references herein,[11] fundamental questions relating to MIC remain unanswered.[5] In particular, little is known about the early steps that initiate corrosion. Traditional models consider degradation kinetics as governed by chemical diffusion and reaction laws. This would imply a quasi-immediate initiation of degradation once bacteria or biofilms are in contact with bare metal.[12,13] However, an effective barrier, an oxide layer that protects the underlying metal from exposure to water and

corrosive substances, can cover the metal. Bacteria would have to damage this protection to break down the passivity layer. Therefore, the early steps remain difficult to predict and observe experimentally at the micrometer scale. For instance, light reflection and absorption by the metal hinder direct observation of bacteria (see for instance refs 14−16 and references herein); alternative scanning electron microscopy has been recently proposed.[17]

Here, we work with nanosheets (or nanofilms) composed of iron nanolayers (Figure 1A). Reactivity and stability of the
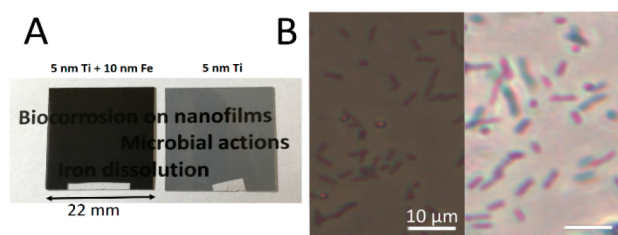

Figure 1. Iron nanofilms. (A) Pictures of gray and semitransparent nanofilm thermally evaporated on glass coverslips. A titanium prelayer (right coverslip), 5 nm thick, warranted an efficient adhesion of the 10 nm thick iron nanofilm in some samples (left coverslip). (B) Bacteria localized at the metal nanofilm surface (left) or on the glass (right) were captured using an inverted phase-contrast microscope.

semitransparent nanofilm are studied in the presence of bacteria at the macro- and microscale levels. Being anaerobic facultative and serving as models in recent research, the wild type iron reducing bacteria (IRB) *Shewanella oneidensis* MR1 are diluted in a rich static liquid medium that favors its growth. Hence, we report one of the first continuous studies of biocorrosion from its initiation to complete dissolution of the metal. Metal and bacteria were visualized with an optical microscope and analyzed *in situ* directly in the liquid medium. Figure 1B displays bacteria that clearly depart from the substrate background in the presence (left) and absence of iron (right panel). Dissolution of the iron substrate increased the transmitted light and image brightness, while bacteria brought clearly distinctive dark objects to the images in the phase-contrast mode. Observations and image analyses were completed with macroscopic optical and electrical measurements capable of recording nanometer thinning and degradation kinetics, together with microscale measurements of pH and oxygen (O_2) concentrations. The quantitative findings issued from experiments on *Shewanella oneidensis* (mostly), *Escherichia coli*, and *Lactobacillus plantarum* (recently renamed *Lactiplantibacillus plantarum*[18]) suggest a positive, temporal correlation between corrosion onset and oxygen depletion combined with iron reduction.

■ RESULTS AND DISCUSSION

Iron Nanosheets and Their Surface Characterization.
The partially transparent metallic film consists of a 10 nm thick iron layer, thermally evaporated, either directly on a microscope glass coverslip or most often on a pre-evaporated 5 nm titanium layer, a typical layer that provides an effective adhesion onto the glass. We verified that the presence or lack of this Ti adhesion layer did not alter the results presented here. Note that iron nanofilm or nanosheet is also termed "ultrathin film" in the literature. Different physical and chemical techniques (optical, electrical, mechanical, and spectroscopic) were used to characterize nanofilm, in particular, its surface. Being a good

compromise, 10 nm of thickness ensures the nanofilm: (1) is transparent (thin) enough to perform optical measurements using an inverted microscope in the phase-contrast mode and to record variations of the transmitted light over a large range of light intensity values (as shown in Supporting Information Appendix, Figure S1A); (2) is thick enough to be composed of a solid Fe[0] layer that shares common features with macroscopic Fe[0] bulk metal in terms of the chemical state and electrical properties (as shown later and in Supporting Information Appendix, Figure S1B). Atomic force microscopy (AFM) allowed us to characterize the nanofilm topography and to establish the presence of a perfectly uniform and smooth (or nanorugose) surface over the micrometer scale of bacteria (Supporting Information Appendix, Figure S1C−D). The chemical state of all atomic elements across the nanofilm surface was then characterized by X-ray photoelectron spectrometry (XPS). Detailed analyses are described in Supporting Information Appendix, Figure S2 and revealed the presence of oxygen only at the surface. Hence, the XPS experiments clearly demonstrate that a uniform nanolayer, i.e. a mostly oxidized iron heterostructure (predominantly composed of Fe(III)), covers the underlying bulk solid metal of the nanofilms; for simplicity, in the subsequent text, this layer will be referred to as an oxide layer. These results are in agreement with the nanocoating properties reviewed in ref 19 and with refs 20 and 21 in which similar nanofilms were studied and where the oxidized iron nanolayers overlaying the Fe(0) metal were found noncrystalline and about 3 nm thick.

Sudden Uniform Degradation and a Concomitant Rise in Electric Current.
Inverted optical microscopy was utilized to observe *in situ* nanosheet degradation at the micron scale in static mode, i.e., without liquid flux. Once bacteria were inoculated at time $t = 0$, we performed real-time observations in phase-contrast mode and recorded image sequencing every 5 or 10 min. In a first attempt, gray values of each pixel on every image were averaged and then analyzed for each sequence; detailed pixel-by-pixel analyses will be presented in subsequent sections. As shown in SI Appendix, Figure S3, the image brightness analyses reveal without ambiguity a uniform and homogeneous corrosion and an intriguing non-monotonic variation, suggestive of the existence of a sudden corrosion onset.

Specific, self-designed macroscopic experiments of optical transmission were performed to quantitatively measure corrosion kinetics. In Figure 2A, photodiode signals recorded from three samples are plotted as a function of time—a high signal indicating a high light level. The first two samples correspond to two reference samples: bacteria alone without nanofilm (green), and nanofilm alone without bacteria in the sterile culture medium (blue). In the former case, the signal decreased monotonically with time (green) due to bacterial growth and consequently to the increasing turbidity of the liquid culture; the corresponding optical density is graduated on the right axis. In the latter curve (blue-filled circles), the signal consistently remains low (about 3.5 V in Figure 2A) over time, indicating constant light absorption and no detectable degradation when immersing the nanofilm into a sterile liquid medium. Figure 2A presents a typical recording (red-filled circles) when bacteria are injected and mixed at time $t = 0$ in a dish containing the liquid medium and the iron nanofilm coverslip. Data variation was not monotonic as suspected previously, and three phases are clearly distinguishable in Figure 2A: (1) an initiation phase without any signal variation that
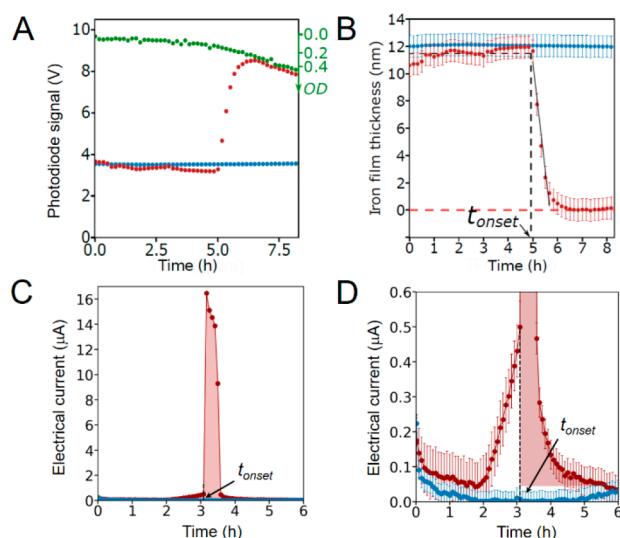
Figure 2. Temporal degradation of a nanofilm as detected by a photodiode mounted in an optical macroscopic setup (A). The calibrated setup allowed us to measure the transmitted light signal (A) and to determine iron film thickness as a function of time (B). Multiplying bacteria also contributed to turbidity as shown by the signal variation on a reference sample without iron nanofilm (green-filled circles in (A)); optical density (OD) of the bacterial solution is graduated on the right axis. Initial bacteria concentration, OD = 0.003. The optical signal was constant when immersing iron nanofilm into liquid medium without bacteria (blue-filled circles in (A, B)), while it varied in the presence of both bacteria and nanofilm (red-filled circles). Metal corrosion onset appeared suddenly at $t = t_{onset}$. Color code in the following figures: green (*Shewanella* alone), blue (nanofilm alone), and red (*Shewanella* + nanofilm). (C−D) Electrical current as measured during metal degradation when connecting the iron nanofilm (without Ti layer) to an ammeter and a platinum counter-electrode half-immersed from the top of the liquid sample. With the sample being placed on the optical setup, we were able to measure both electrical and optical signals *in situ* simultaneously. Metal dissolution also appeared suddenly. Initial OD = 0.03. (C) As measured by the ammeter, relatively large electron flows (more than 10 μA) were produced concomitantly with metal dissolution (red-filled circles). Note that only absolute values of the negative current are plotted in (C−D). Summing the intensity values in a definite integral (red area) leads us to estimate a total charge flowing through the circuit equal to 0.045 C, close to 0.066 C, the charge expected when roughly assuming one electron transfer per dissolved iron atom. (D) The magnified figure reveals early variations of the low current values before optical semitransparency began to change suddenly at $t = t_{onset}$.

lasted a few hours; (2) a degradation phase during which the signal increased, and (3) a postdegradation phase when the signal decreased as it did in the bacterial reference sample due to bacterial growth. Corrosion kinetics are extracted from the signal using calibration curves and removing the bacterial contribution. In Figure 2B, the nanofilm thickness is shown as a function of time. At a nanometer resolution, a spatial resolution was optically attainable thanks to the exponential dependence of light absorption with thickness and to the high absorption coefficient of iron (SI Appendix, Figure S1A). The corrosion onset appeared suddenly at $t = t_{onset}$ and followed a complete metal dissolution within 1−2 h. The corrosion rate rose abruptly and reached a constant value equal to 11 ± 3 nm/h (or equivalently 0.10 mm/y)—a value averaged over all sample values (Supporting Information Appendix, Corrosion rates and the suspected abiotic corrosion)—and then decreased when

approaching the last metal layers. This value agrees with the data reported in the literature (read for instance ref 22).

As electrochemical reactions and consecutive electron transfers induce iron dissolution, it is possible to detect the corrosion event by measuring the electric current. Figure 2C displays the results recorded on one sample with (red) and one without bacteria (absolute values, blue-filled circles). The electric current of the latter remained constant and low (<0.2 μA) over time. By contrast, in the presence of bacteria, a degradation phase of a high current level (>0.5 μA) was found to surround both the initiation and postdegradation phases of the low current level. The sudden nanofilm thinning (optically measured on the same sample) that defined $t = t_{onset}$ was found concomitant with the sudden rise in the electric current. The directional current flow allowed us to conclude that electrons were flowing from the iron nanofilm to the platinum counter-electrode, suggesting an anodic metal dissolution—as would be expected for a "strict" corrosion—coupled to a reduction at the counter-electrode; the nanofilm degradation is therefore corrosion. As seen in Figure 2C, the current suddenly reaches 15−20 microamperes and then drops by 90% at the end of the thinning process. The magnified Figure 2D shows the small current values for clarity and displays a slow and weak increase of the electric current 1 h before the corrosion onset. This period of early weak electroactivity which lasted between 30 min and 1 h and 30 min—noted 1/2 and 1 h 30 in this study—depending on the sample, was not detectable from optical signals that instead, remained constant, suggesting no change in the solid Fe(0) layer thickness during this electroactive period.

Next, we measured the open circuit potential (OCP) using a voltmeter connected to the nanofilm and to an Ag/Ag−Cl counter-electrode immersed in the liquid medium (SI Appendix, Figure S4). Reference samples exhibited low and constant voltage values (−60 ± 40 mV), indicating a relatively stable passive state of the oxidized iron nanolayers over long periods. By contrast, sudden rises in negative OCP values associated with the sudden rise in current were clearly observed at $t = t_{onset}$. An abrupt drop at about −600 mV signals the passivity breakdown. Corrosion onset quickly followed an early progressive decrease to −225 ± 60 mV (on average) signaling early progressive surface modifications.

In order to interpret these data, we measured the electrical properties of a bulk iron sheet (0.1 mm thick) under the same conditions. The sheet was previously exposed to ambient air and humidity and showed no visible signs of rust or oxidation. Just after its immersion into sterile liquid medium (without bacteria), the sheet started to corrode. A current of 10−20 μA (vs Pt) and a corrosion voltage of −650 mV (vs Ag/AgCl) were detected quasi-immediately and over long periods (SI Appendix, Figure S5). These readings indicate the rapid instability of the oxide covering of the bulk thick metal compared to the stability of the oxidized iron overlaying the Fe(0) nanolayers and confirms that the nanocoatings are able to reduce the effect of a corrosive environment.[19] Furthermore, the similar OCP values suggest that nanofilm with bacteria corrodes like thick metal without bacteria. In both cases, the electrochemical reactions could occur at the solid Fe(0) metal−liquid medium surface and drive the corrosion without the possible regeneration of an oxide layer sufficiently passive to protect the underlying metal. These reactions lead to the oxidation of the metal and its progressive dissolution together with the electron flow from the oxidized metal, through the electrical wire and up to the platinum

electrode where reduction occurred (SI Appendix, Corrosion rates and the suspected abiotic corrosion).

Surface Density, Localization, and Dynamics of Bacteria. While the corrosion onset time was easily extracted from the mean gray values, detailed and quantified studies of bacteria density and dynamics require more advanced image processing. The one-looped Supporting Information Appendix, Movie S1 shows six sequences of 50 images recorded every 30–50 ms. Figure 3A displays an example of image processing leading to Movie S1; starting from the initial dark picture on the left, a renormalization using thresholds led to the middle picture where gray levels have been inverted. Movie S1 provides considerable information on bacterial shape, dynamics, and surface distribution before and after the corrosion onset. A first visual inspection indicates that bacteria were homogeneously distributed on the surface over time. Few filamentous cells and no biofilm clusters were visible within the 4 h period that followed the inoculation—a pellicular biofilm being seen 12–24 h later. Instead, individual growing cells were the most abundant population regardless of the samples.

Image analyses allowed us to unambiguously determine the bacterial surface density (per unit area), the area fraction calculated by dividing the area covered by the detected bacteria on each image by the total image area (SI Appendix, Figure S6). Figure 3B shows the surface density of two incubated bacterial samples, one without (left) and one with metal nanofilm (right plot). Overall, no precise value nor unique law governing cell numbers at the surface was observed, and their global number weakly increased with incubation time. However, the cells' density of some samples presented a sudden non-monotonic change just after corrosion onset; this non-monotonic change will be discussed in the next paragraph. Depending on the sample (Supporting Information Appendix, Figure S6), the corrosion process began at very different t_{onset} values (from 1 to 3 h) and at very different surface density values, further noted σ_s^{onset} (from 10 to 45%). As shown on the same scatter plot in Figure 3C, data ($t_{onset}, \sigma_s^{onset}$) may form two unexpected distinct groups that are aligned to two distinct oblique and quasi-parallel straight lines, meaning two clusters have linear positive correlation; many experiments will be needed to distinguish the possible correlation.

The two most striking observations in Supporting Information Appendix, Movie S1 are (1) the absence of motility of some cells standing over the metal nanofilm—immobilized and motionless cells are named sessile bacteria in the following text—associated with the early period of weak electroactivity; (2) in contrast, the presence of many single and rapidly moving bacteria appearing just after the corrosion onset. (1) A first quantitative and detailed sessility analysis, in terms of localization function, is proposed in Supporting Information Appendix, Figure S7, and it reveals an almost complete renewal or surface regeneration of bacteria during the initiation phase. Bacteria located at or near the metal or glass surface were not attached strongly enough to the surface to remain localized on the same site. Many newly incoming bacteria recolonized the surface during the whole phase. A similar lack of cells' affinity for glass and for solid metal clearly appeared. (2) By contrast, the previous nonmonotonic change in surface density quantified a sudden influx of rapidly moving bacteria seen in Supporting Information Appendix, Movie S1. The iron, being progressively released and solubilized as soon as the corrosion started, generated a local iron concentration gradient that was most likely detected by bacteria, directing their motions toward the
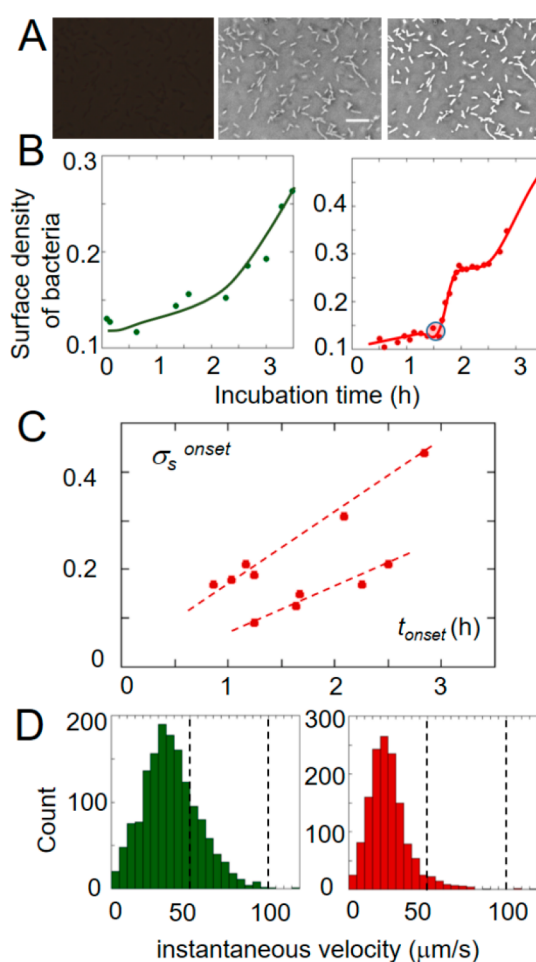

Figure 3. Surface density and dynamics of bacteria in contact with, or nearby, the iron nanofilm as detected by digital image processing and analysis. (A) Bacteria are clearly visible on the center picture when processing thresholding and renormalization of the initial left image. Scale bar = 20 μm. On the right image, bacterial areas, as detected by image segmentation and binarization, are white-colored and superimposed over bacteria observed on the original middle image. Initial OD = 0.07. (B) Surface densities of bacteria, calculated from the white areas and denoting the area covered by cells per unit area, are plotted as functions of time. Bacterial areas of two representative samples were measured: a reference sample where bacteria were in contact with the glass coverslip (the left plot, dark green-filled circles); one sample with iron nanofilm exhibiting a different density curve (the right plot, red-filled circles). The time t_{onset} of corrosion onset, deduced from the mean gray value, is marked by a semitransparent colored disk. Curved continuous lines are simply guides for the eyes. Initial OD = 0.07. (C) The bacterial surface density (per unit area) measured at $t = t_{onset}$ on different samples is plotted as a function of t_{onset} (details in Figure S6). Data could split in two clusters with a positive linear correlation, as indicated by the two dashed red lines. (D) Histograms of the bacterial instantaneous velocity deduced from tracking: (1) left histogram (green bars): velocities of long runs when bacteria—freshly removed from the incubator shaker and diluted—swam in the oxygenated liquid culture; (2) right histogram (red bars): velocities of bacterial rapid motions and short runs observed just after the corrosion onset. The weak difference in the mean velocity might come from the constrained environment where bacteria were densely moving near the metallic surface; a decreased velocity was caused by collisions with one another.

rich region surrounding the dissolving nanofilm, as already reported in refs 23 and 24 and in ref 25 for *Geobacter metallireducens*. Every bacterium was highly dynamic, and all
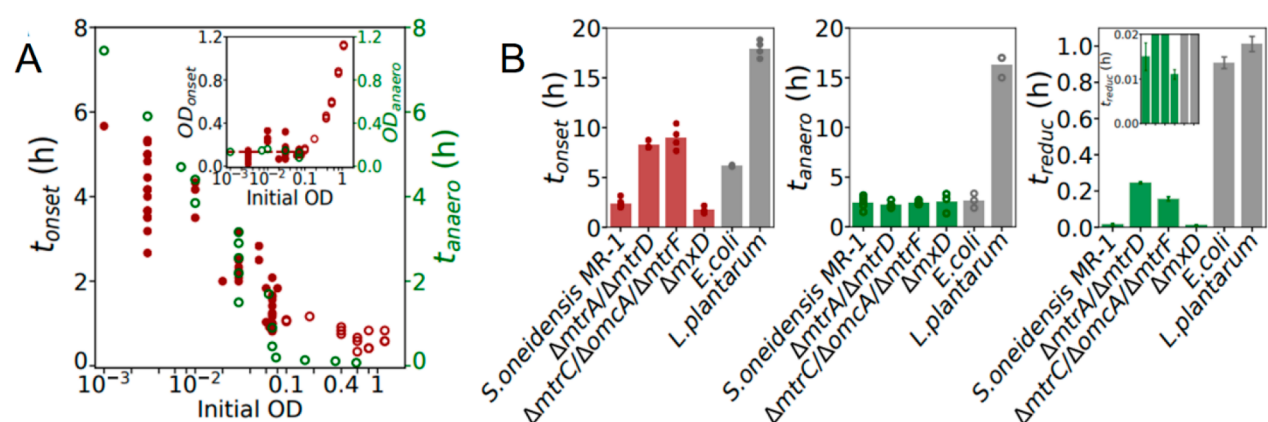
Figure 4. Environmental and microbiological factors influencing the time of corrosion onset. (A) Duration of the initiation phase, as defined by t_{onset} and reported on the left vertical axis, depended on the initial bacterial concentration, which was quantified by the initial optical density (OD) of the liquid culture. In the inset, the mean macroscopic OD_{onset} values reached at $t = t_{onset}$ are plotted on the left ordinate axis as a function of the initial OD. Comparison between t_{onset} and t_{anaero} or between OD_{onset} and OD_{anaero} with t_{anaero} and OD_{anaero} (graduated on the right vertical axes and denoting, respectively, the time and mean optical density needed to reach a strict anaerobic environment nearby the metal nanofilms). Two concentration regimes clearly appeared: (1) when the samples were already highly concentrated, two constant periods of incubation 45 ± 15 min and, a few minutes, irrespective of the samples, were required to observe corrosion (red-empty circles) and full-O_2 depletion (green-empty circles) respectively. (2) When starting from a diluted bacterial concentration, bacteria grew until they reached a constant bacterial concentration (0.13 ± 0.06; dashed line in the inset) sufficient enough to enable the transition toward corrosion (red-filled circles) and to fully and locally deplete oxygen (green-empty circles). (B) Three characteristic times measured or calculated for four *S. oneidensis* strains (t_{onset}, red-filled circles and bars; t_{anaero} and t_{reduc}, green-filled circles and bars) and for the two other species, *E. coli* WT and *L. plantarum* (gray-filled circles and bars). Here t_{onset} and t_{anaero} are the two first characteristic times directly measured on all the strains and species. Initial OD = 0.03. Knowing that the liquid medium contains about 10 μM of soluble iron (more exactly 17 μM),[27] the third characteristic time corresponds to the time t_{reduc} required for reducing 10 μM of soluble iron(III) at a k_{reduc} rate. Kinetics of iron(III) reduction were quantified separately in order to determine the different k_{reduc} values of the reduction rate; data are reported on Supporting Information Appendix, Figure S10.

local motions were rapid. A histogram of the instantaneous velocities is plotted on the right side of Figure 3D, and the mean velocity value is found to be equal to 25 ± 13 μm/s. This value is close to 38 ± 18 μm/s, the mean velocity value that was measured when diluted *S. oneidensis* performed long runs in freshly oxygenated medium (histogram on the left).

Iron Reduction in a Local Anaerobic Environment. We varied environmental and microbiological parameters in order to determine the triggering events that stimulated passivity breakdown. Initial bacterial densities were first modified and, regardless of the initial bacterial concentrations, corrosion was found uniform and sudden. All t_{onset} values are plotted in a semilogarithmic graph in Figure 4A in which two concentration regimes appear. In the first regime, at high initial OD values (>0.1), the t_{onset} values are independent of the initial conditions, and on average, corrosion began at $t_{onset} = 45 \pm 15$ min. In the second regime, when initial cells were highly diluted (OD < 0.1), passivity breakdown was delayed; in Figure 4A, all t_{onset} values globally decrease linearly following a logarithmic scale relationship which suggests a global bacterial growth effect. Monitoring in parallel the turbidity of bacterial samples without nanofilm allowed us to determine the liquid solution OD values reached at any time and in particular at $t = t_{onset}$—assuming that the nanofilm did not modify the bacterial growth in the bulk. The corresponding OD values reached at $t = t_{onset}$, termed OD_{onset}, are plotted as a function of the initial OD in the Figure 4A inset; we found an average value equal to $OD_{onset} = 0.13 \pm 0.06$ (equivalent to 10^8 colony-forming-units/mL). Hence, during the early initiation phase, we know that, on one hand, bacteria multiplied up to a minimum concentration indicating a potential quorum sensing effect and/or activation of a different metabolic pathway. On the other hand, some progressive electrochemical reactions modify the oxide layer and its environment. Additional

experiments indicated that direct bacteria−nanofilm contacts were absolutely needed during this early initiation phase (Supporting Information Appendix, Separated compartments). This result can be related to other reports obtained in conditions relevant to biofilms in the future.[26]

As iron reducing bacteria, like *S. oneidensis*, are known to respire insoluble metals only under anaerobic conditions, we first monitored O_2 levels of the bacterial microenvironment surrounding a glass coverslip using a microsensor in samples of different initial concentrations. Supporting Information Appendix, Figure S8 depicts three oxygen-depletion kinetics. As suspected, oxygen was locally depleted within 5 min to 6 h following the inoculation depending on the initial bacteria concentration. These t_{anaero} sample values are reported in Figure 4A and are compared to the t_{onset} values. Interestingly, both values are very similar in the second concentration regime (low initial OD values < 0.07) supporting the idea of a strong correlation between anaerobic conditions and corrosion onset. In the first concentration regime (initial OD values > 0.07−0.1) however, values differ: if oxygen was rapidly depleted in less than 10 min, 45 min were required to initiate corrosion. Thus, the results indicate that metal corrosion observed on all samples occurred in an almost strictly anaerobic environment where iron respiration may have occurred, and an additional period of anaerobic incubation was needed to trigger the degradation. If this additional period was not sufficiently long enough for cells to duplicate, it did allow them to express the necessary genes involved in the interaction with the iron oxide surface. This additional period prior to the corrosion onset is consistent with the duration of the early electroactive period noticed before. At $t = t_{anaero}$, the bacterial concentration of a few samples OD_{anaero} in the second regime was also measured using a spectrophotometer, and the results are shown in the Figure 4A inset. Again,

OD_{onset} and OD_{anaero} values are identical, demonstrating the need for reaching a minimal and global bacterial density to fully deplete oxygen from the local environment of metal nanofilms and to enable their passivity breakdown.

We further noticed a significant delay in corrosion onset upon addition of soluble extra-iron Fe(III) to the medium (Supporting Information Appendix, Figure S9), reinforcing the importance of microbial respiration in the triggering event and interplay between soluble and insoluble iron reduction. As the culture medium itself contained an initial amount of soluble iron molecules (of the order of 10−20 μM concentration, too low to be measured in our conditions[27]), the initial soluble iron was then suspected to interplay with the reduction of the insoluble Fe(III) oxides located at the nanosheet surface. The reduction kinetics, in itself, was then measured in separate experiments under conditions mimicking the local nanofilms' environment (anaerobic and OD = 0.1) and in the presence of soluble Fe(III) ammonium citrate molecules (10 mM); abiotic controls indicated no significant amount of reduced iron. As displayed in Supporting Information Appendix, Figure S10, a linear fit of the first reduced Fe(II) concentrations versus time allowed us to determine the reduction rate k_{reduc} and the related time t_{reduc}. This time, t_{reduc} corresponds to the time that would be required for bacteria to reduce the few soluble iron molecules present in the liquid culture (10 μM) at the rate k_{reduc}, i.e., without considering the complex environment of the standing culture in aerobic atmosphere and the limiting diffusion of diluted iron molecules. To summarize, the three different characteristic times (t_{onset}, t_{anaero}, and t_{reduc}) determined on *S. oneidensis* WT and on three mutants are reported on three graphs in Figure 4B. The MtrC, OmcA, and MtrF decaheme c-type cytochromes (the terminal electron donors within the external membrane) are deprived in the first mutant, impeding the outer traditional electron pathway that reduces iron oxides, while the MtrA and MtrD decaheme c-type cytochromes that facilitate internal electron transfers to the other previous outer membrane cytochromes are deleted in the second mutant.[28] Mutations significantly delayed reduction time and corrosion onset unlike the mutation of the third mutant unable to synthesize extracellular polysaccharides.[29] This result clearly demonstrates: (i) c-cytochromes of the Mtr pathway are implicated in nanofilm corrosion initiation; (ii) the two mutants were able to interact with iron using alternative and less efficient pathways, reflecting the extraordinary respiratory versatility of *S. oneidensis*;[30,31] (iii) a positive temporal correlation between corrosion onset and soluble iron reduction, the time of corrosion onset being less impacted by the mutations than the reduction time—such a difference might be related to the secretion of extracellular flavins, molecules considered as electron shuttles that preferentially facilitate the reduction of soluble iron rather than insoluble iron;[32,33] (iv) the polysaccharide matrix was not implicated in the corrosion process under our short-term experimental conditions.

Finally, the last series of experiments were done on two other facultative anaerobes different from iron reducing bacteria, *Escherichia coli* and *Lactobacillus plantarum*. As reported by Logan et al. in a recent review (see also the references herein[34]), *E. coli* is often used as a negative control, nonexoelectrogen, i.e., not equipped with the membrane proteins chain permitting external electron transfers (EET). Though not being able to respire external insoluble iron unlike IRB, *E. coli* cells need iron for metabolism like most living cells, and few studies discriminate the dissimilation from assimilation processes (see,

for instance, ref 35). By contrast, *L. plantarum* is one exception of living cells that do not (or very little) depend on iron[1,36] but do contain genes for EET (not all) as recently reported.[37] Its ability to reduce external soluble Fe(III) was found close to nil (but non nil) and to correspond to the lowest activity across part of the Firmicutes phylum.[37] All results are summarized in Figure 4B and indicate that, although not being as efficient as *S. oneidensis*, both (*E. coli* and *L. plantarum*) enabled the transition toward the corrosion process. Supplementary analyses suggest a passivity breakdown mediated by small secreted soluble compounds like molecular shuttles and byproducts of *E. coli* fermentation rather than direct contacts in agreement with ref 38 (Supporting Information Appendix, Separated compartments) and related to the acidic environment of *L. plantarum* (measured using microsensors) (Supporting Information Appendix, Figure S11).

Note that corrosion rates performed on mutants and on the two other species are shown in (Supporting Information Appendix, Figure S12) and discussed in (Supporting Information Appendix, Corrosion rates and the suspected abiotic corrosion).

Hence, transformation and dissolution of environing iron are remarkable common features shared by a number of bacterial species, as suggested by the present experiments and by previous studies (see for instance, refs 34 and 39). Our present experiments, based on microscopic observations through an iron nanofilm, allows us to monitor initial stages and to display positive temporal correlations between corrosion onset and oxygen depletion combined with iron reduction. Further detailed studies could permit the identification of mechanisms responsible for passivity breakdown. The early steps of matter transformation, being interfacial, nanometer-thin materials, may offer new insight into elucidating bacterial actions within other processes, such as plastic biodegradation and solid pollutant bioremediation, and new perspectives into nanocoatings capable of improving materials' functionalities.

■ MATERIALS AND METHODS

Iron Nanofilm Processing/Preparation. See Supporting Information Appendix, Iron nanofilm processing/preparation.

AFM Measurements. See Supporting Information Appendix, AFM measurements.

Bacterial Strain and Growth Conditions. Wild type *Shewanella oneidensis* strain MR-1 (LGC Standards), the deleted mutants JG594 (ΔmtrA/ΔmtrD),[28] JG596 (ΔmtrC/ΔomcA/ΔmtrF),[28] and (ΔmxD)[29] were cultured similarly. Single colonies were obtained by isolation from frozen stocks on Luria Broth (LB) agar plates and inoculated into 5 mL of liquid LB, shaken for 18 h at 200 rpm at 30 °C for overnight cultures. Then, typical dilutions (1:1000) in LB from overnight culture were completed. Most bacteria were picked up at the beginning of the exponential phase when OD ≈ 0.1 and then diluted in LB in one of the different culture chambers. The optical density (OD) measured at 600 nm provided an estimation of the cell concentration in each sample; OD values were calibrated to colony-forming-units (cfu) by spreading multiple dilutions on agar plates and counting the number of colonies: 1 OD = 7×10^8 cells/mL. All experiments presented here were done at 23−25 °C. At the end of each experiment, culture purity was controlled by analyzing the colonies' morphology obtained after a streaking in an LB plate.

A bottomless and topless culture chamber made of glass-filled PTFE and suitable for use with an inverted microscope (ZEISS

Primovert) was designed and machined at the laboratory. After the nanofilm's coverslip was placed and sealed at the bottom, the chamber was filled from the top with 2.5 mL of bacterial culture in a sterile cabinet and covered with a classical glass coverslip. Optical and electrical experiments were performed in small Petri dishes (50×20 mm), immersing the nanofilm's coverslip to the dish's bottom into 10 mL of liquid culture.

No unexpected or unusually high safety hazards were encountered.

Optical Macroscopic Measurements. See Supporting Information Appendix, Optical macroscopic measurements.

Electrical Measurements. See Supporting Information Appendix, Electrical measurements.

Microscopic Measurements of pH and Oxygen (O₂) Concentration. See Supporting Information Appendix, Microscopic measurements of pH and oxygen (O_2) concentration.

Iron Reduction − Ferrozine Assay. See Supporting Information Appendix, Iron Reduction − Ferrozine assay.

◾ ASSOCIATED CONTENT

Ⓢ Supporting Information

The Supporting Information is available free of charge at https://pubs.acs.org/doi/10.1021/acscentsci.1c01126.

A one-looped and slow motion movie showing six sequences recorded before and during the corrosion (MP4)

Corrosion rates and the suspected abiotic corrosion; separated compartments; iron nanofilm processing/preparation; AFM measurements; XPS measurements; optical macroscopic measurements electrical measurements; microscopic measurements of pH and oxygen (O_2) concentration; iron reduction − ferrozine assay; supplementary figures: Figure S1: Some physical properties of iron nanofilms. Figure S2: Spectra of X-ray photoelectron spectrometry. Figure S3: Temporal degradation of a nanofilm as observed by optical microscopy. Figure S4: Open circuit potential measured during the nanofilm degradation. Figure S5: Electrical signals measured during the bulk iron degradation. Figure S6: Temporal variations of bacterial surface density. Figure S7: Cells' dynamics and sessility analysis. Figure S8: Kinetics of oxygen (O_2) depletion. Figure S9: Delay in the corrosion onset upon addition of soluble Fe(III). Figure S10: Kinetics of iron(III) reduction. Figure S11: Temporal variations of local pH. Figure S12: Corrosion rates (PDF)

◾ AUTHOR INFORMATION

Corresponding Author

Eric Raspaud − *Université Paris-Saclay, CNRS, Laboratoire de Physique des Solides, 91405 Orsay, France;* ⓞ orcid.org/0000-0002-9511-8479; Email: eric.raspaud@universite-paris-saclay.fr

Authors

Marion Lherbette − *Université Paris-Saclay, CNRS, Laboratoire de Physique des Solides, 91405 Orsay, France*

Christophe Regeard − *Institute for Integrative Biology of the Cell (I2BC), Université Paris-Saclay, CEA, CNRS, 91198 Gif-sur-Yvette, France*

Christian Marlière − *Université Paris-Saclay, CNRS, Laboratoire de Physique des Solides, 91405 Orsay, France*

Complete contact information is available at:
https://pubs.acs.org/10.1021/acscentsci.1c01126

Notes

The authors declare no competing financial interest.

◾ REFERENCES

(1) Andrews, S. C.; Robinson, A. K.; Rodríguez-Quiñones, F. Bacterial iron homeostasis. *FEMS Microbiol. Rev.* **2003**, *27*, 215−237.

(2) Ilbert, M.; Bonnefoy, V. Insight into the evolution of the iron oxidation pathways. *Biochim. Biophys. Acta, Bioenerg.* **2013**, *1827*, 161−175.

(3) Hochella, M. F., Jr; Lower, S. K.; Maurice, P. A.; Penn, R. L.; Sahai, N.; Sparks, D. L.; Twining, B. S. Nanominerals, mineral nanoparticles, and earth systems. *Science* **2008**, *319*, 1631−1635.

(4) Flemming, H.-C. *Microbially Influenced Corrosion of Materials - Scientific and Technological Aspects*; Heitz, E.; Sand, W.; Flemming, H.-C., Eds.; Springer, Heidelberg, 1996; pp 5−14.

(5) Little, B. J.; Blackwood, D. J.; Hinks, J.; Lauro, F. M.; Marsili, E.; Okamoto, A.; Rice, S. A.; Wade, S. A.; Flemming, H.-C. Microbially influenced corrosion − Any progress? *Corros. Sci.* **2020**, *170*, 108641.

(6) Nace International, 2016. http://impact.nace.org/economic-impact.aspx.

(7) Lewandowski, Z.; Beyenal, H. In *Marine and Industrial Biofouling*; Flemming, H.-C., Murthy, P. S., Venkatesan, R., Cooksey, K. E., Eds.; Springer-Verlag: Berlin Heidelberg, 2009; pp 35−65.

(8) Flemming, H.-C.; Geesey, G. G. Biofouling and Biocorrosion in Industrial Water Systems. In *Proceedings of the International Workshop on Industrial Biofouling and Biocorrosion*; Stuttgart, 1990.

(9) Borenstein, S. B. *Microbiologically Influenced Corrosion Handbook*; Industrial Press: New York, 1994.

(10) Iverson, W. P. Microbial corrosion of metals. *Adv. Appl. Microbiol.* **1987**, *32*, 1−36.

(11) Stott, J. F. D. What progress in the understanding of microbially induced corrosion has been made in the last 25 years? A personal viewpoint. *Corros. Sci.* **1993**, *35* (1−4), 667−673.

(12) Melchers, R. E.; Wells, T. Models for the anaerobic phases of marine immersion corrosion. *Corros. Sci.* **2006**, *48*, 1791−1811.

(13) Marciales, A.; Peralta, Y.; Haile, T.; Crosby, T.; Wolodko, J. Mechanistic microbiologically influenced corrosion modeling- a review. *Corros. Sci.* **2019**, *146*, 99−111.

(14) Wang, Y.; Cheng, G.; Li, Y. Observation of the pitting corrosion and uniform corrosion for X80 steel in 3.5% NaCl solutions using in-situ and 3D measuring microscope. *Corros. Sci.* **2016**, *111*, 508−517.

(15) Yuan, B.; Li, Z.; Tong, S.; Li, L.; Wang, C. In Situ Monitoring of Pitting Corrosion on Stainless Steel with Digital Holographic Surface Imaging. *J. Electrochem. Soc.* **2019**, *166*, C3039.

(16) Sander, G.; Cruz, V.; Bhat, N.; Birbilis, N. On the in-situ characterization of metastable pitting using 316L stainless steel as a case study. *Corros. Sci.* **2020**, *177*, 109004.

(17) Iannucci, L.; Lombardo, L.; Parvis, M.; Cristiani, P.; Bosséguy, R.; Angelini, E.; Grassini, S. *2019 IEEE International Instrumentation & Measurement Technology Conference*; Auckland, New Zealand, May 2019.

(18) Zheng, J. A taxonomic note on the genus *Lactobacillus*: Description of 23 novel genera, emended description of the genus *Lactobacillus Beijerinck 1901*, and union of *Lactobacillaceae* and *Leuconostocaceae*. *Int. J. Syst. Evol. Microbiol.* **2020**, *004107*, 1−77.

(19) Abdeen, D. H.; El Hachach, M.; Koc, M.; Atieh, M. A. Review on the Corrosion Behaviour of Nanocoatings on Metallic Substrates. *Materials* **2019**, *12*, 210.

(20) Boamah, M. D.; Lozier, E. H.; Kim, J.; Ohno, P. E.; Walker, C. E.; Miller, T. F., III; Geiger, F. M. Energy conversion via metal nanolayers. *Proc. Natl. Acad. Sci. U. S. A.* **2019**, *116*, 16210−16215.

(21) Faurie-Wisniewski, D.; Geiger, F. M. Synthesis and character-ization of chemically pure nanometer-thin zero-valent films and their surfaces. *J. Phys. Chem. C* **2014**, *118*, 23256−23263.

(22) Féron, D.; Crusset, D. Microbial induced corrosion in French concept of nuclear waste underground disposal. *Corros. Eng., Sci. Technol.* **2014**, *49*, 540−547.

(23) Harris, H. W.; Sanchez-Andrea, I.; McLean, J. S.; Salas, E. C.; Tran, W.; El-Naggar, M. Y.; Nealson, K. H. Redox sensing within the genus *Shewanella*. *Front. Microbiol.* **2018**, *8*, 2568.

(24) Harris, H. W.; El-Naggar, M. Y.; Bretschger, O.; Ward, M. J.; Romine, M. F.; Obraztsova, A. Y.; Nealson, K. H. Electrokinesis is a microbial behavior that requires extracellular electron transport. *Proc. Natl. Acad. Sci. U. S. A.* **2010**, *107*, 326−331.

(25) Childers, S. E.; Ciufo, S.; Lovley, D. R. *Geobacter metallireducens* accesses insoluble Fe(III) oxide by chemotaxis. *Nature* **2002**, *416*, 767−769.

(26) Lies, D. P.; Hernandez, M. E.; Kappler, A.; Mielke, R. E.; Gralnick, J. A.; Newman, D. K. *Shewanella oneidensis* MR-1 uses overlapping pathways for iron reduction at a distance and by direct contact under conditions relevant for biofilms. *Appl. Environ. Microbiol.* **2005**, *71*, 4414−4426.

(27) Abdul-Tehrani, H.; et al. Ferritin mutants of *Escherichia coli* are iron deficient and growth impaired, and fur mutants are iron deficient. *J. Bacteriol.* **1999**, *181*, 1415−1428.

(28) Coursolle, D.; Gralnick, J. A. Modularity of the Mtr respiratory pathway of *Shewanella oneidensis strain MR-1*. *Mol. Microbiol.* **2010**, *77*, 995−1008.

(29) Gambari, C.; Boyeldieu, A.; Armitano, J.; Méjean, V.; Jourlin-Castelli, C. Control of pellicle biogenesis involves the diguanylate cyclases PdgA and PdgB, the c-di-GMP binding protein MxdA and the chemotaxis response regulator CheY3 in *Shewanella oneidensis*. *Environ. Microbiol.* **2019**, *21*, 81−97.

(30) Breuer, M.; Rosso, K. M.; Blumberger, J. Electron flow in multiheme bacterial cytochromes is a balancing act between heme electronic interaction and redox potentials. *Proc. Natl. Acad. Sci. U. S. A.* **2014**, *111*, 611−616.

(31) Meyer, T. E.; Tsapin, A. I.; Vandenberghe, I.; de Smet, L.; Frishman, D.; Nealson, K. H.; Cusanovich, M. A.; van Beeumen, J. J. Identification of 42 possible cytochrome C genes in the *Shewanella oneidensis* genome and characterization of six soluble cytochromes. *OMICS* **2004**, *8*, 57.

(32) Ruebush, S. S.; Brantley, S. L.; Tien, M. Reduction of soluble and insoluble iron forms by membrane fractions of *Shewanella oneidensis* grown under aerobic and anaerobic conditions. *Appl. Environ. Microbiol.* **2006**, *72*, 2925−2935.

(33) Kotloski, N. J.; Gralnick, J. A. Flavin electron shuttles dominate extracellular electron transfer by *Shewanella oneidensis*. *mBio* **2013**, *4*, e00553−12.

(34) Logan, B. E.; Rossi, R.; Ragab, A.; Saikaly, P. E. Electroactive microorganisms in bioelectrochemical systems. *Nat. Rev. Microbiol.* **2019**, *17*, 307.

(35) Appenzeller, B. M. R.; Yanez, C.; Jorand, F.; Block, J.-C. Advantage provided by iron for *Escherichia coli* growth and cultivability in drinking water. *Appl. Environ. Microbiol.* **2005**, *71*, 5621−5623.

(36) Archibald, F. *Lactobacillus plantarum*, an organism not requiring iron. *FEMS Microbiol. Lett.* **1983**, *19*, 29−32.

(37) Light, S. H.; et al. A flavin-based extracellular electron transfer mechanism in diverse Gram-positive bacteria. *Nature* **2018**, *562*, 140.

(38) McKinlay, J. B.; Zeikus, J. G. Extracellular ion reduction is mediated in part by neutral red and hydrogenase in *Escherichia coli*. *Appl. Environ. Microbiol.* **2004**, *70*, 3467.

(39) Lovley, D. R. Microbial Fe(III) reduction in subsurface environments. *FEMS Microbiol. Rev.* **1997**, *20*, 305−313.